PNAS RESEARCH ARTICLE | ENVIRONMENTAL SCIENCES

Utilizing the oxygen-atom trapping effect of Co_3O_4 with oxygen vacancies to promote chlorite activation for water decontamination

Ruidian Su[a], Yixuan Gao[b], Long Chen[b], Yi Chen[a], Nan Li[c], Wen Liu[b,1], Baoyu Gao[a], and Qian Li[a,1]

Edited by Alexis Bell, University of California, Berkeley, CA; received November 6, 2023; accepted January 30, 2024

Heterogeneous high-valent cobalt-oxo [≡Co(IV)=O] is a widely focused reactive species in oxidant activation; however, the relationship between the catalyst interfacial defects and ≡Co(IV)=O formation remains poorly understood. Herein, photoexcited oxygen vacancies (OVs) were introduced into Co_3O_4 (OV-Co_3O_4) by a UV-induced modification method to facilitate chlorite (ClO_2^-) activation. Density functional theory calculations indicate that OVs result in low-coordinated Co atom, which can directionally anchor chlorite under the oxygen-atom trapping effect. Chlorite first undergoes homolytic O–Cl cleavage and transfers the dissociated O atom to the low-coordinated Co atom to form reactive ≡Co(IV)=O with a higher spin state. The reactive ≡Co(IV)=O rapidly extracts one electron from ClO_2^- to form chlorine dioxide (ClO_2), accompanied by the Co atom returning a lower spin state. As a result of the oxygen-atom trapping effect, the OV-Co_3O_4/chlorite system achieved a 3.5 times higher efficiency of sulfamethoxazole degradation (~0.1331 min^{-1}) than the pristine Co_3O_4/chlorite system. Besides, the refiled OVs can be easily restored by re-exposure to UV light, indicating the sustainability of the oxygen atom trap. The OV-Co_3O_4 was further fabricated on a polyacrylonitrile membrane for back-end water purification, achieving continuous flow degradation of pollutants with low cobalt leakage. This work presents an enhancement strategy for constructing OV as an oxygen-atom trapping site in heterogeneous advanced oxidation processes and provides insight into modulating the formation of ≡Co(IV)=O via defect engineering.

photoexcited oxygen vacancy | chlorite activation | oxygen atom trapping effect | heterogeneous high-valent cobalt-oxo | ultraviolet modification

Heterogeneous advanced oxidation processes (AOPs) catalyzed by transition metal catalysts have received growing attention in water purification owing to the high reactivity of radicals (i.e., $HO^{\cdot}$ and $SO_4^{\cdot-}$) toward organic pollutants. However, the overlooked reactive sites on the catalyst surface, such as surface high-valent metal species (1–4), metastable oxidant-catalyst complexes (5), and interfacial electron donors (6), also contribute significantly to the oxidation of recalcitrant pollutants. High-valent metal species possess high redox potential (>1.95 V), long half-lifetime (up to several seconds), and unique selectivity [oxygen atom transfer (OAT) oxidation pathway] (7), showing an oxidative effect comparable to radicals. In addition, high-valent metal species are also important intermediates in oxidative transformation processes, such as oxygen activation and chlorite (ClO_2^-) dismutation (8). For example, in the chlorite activation process, high-valent cobalt-oxo [Co(IV)=O] not only dominates the selective degradation of pollutants but also triggers chlorite activation to produce chlorine dioxide (ClO_2) (9). Low-valent cobalt accepts oxygen atoms from chlorite to form Co(IV)=O, which then efficiently activates chlorite to ClO_2 via electron transfer (ET) (10). Benefiting from Co(IV) and ClO_2, chlorite activation has been developed as a selective oxidation technique for targeted degradation of pollutants (9). Thus, the presence of Co(IV)=O plays a crucial role in the activation of chlorite and degradation of pollutants.

However, homogeneous Co(IV)=O is unstable because of the strong electronic repulsion between the *d*-electron of the cobalt center and the electron of oxygen (11), which restricts the sustainable activation of chlorite. Recent studies have revealed that heterogeneous high-valent metal species are more stable and longer-lived (up to several hours) (12). This discovery is considered a breakthrough to improve the activation efficiency of chlorite. Cobalt oxide (Co_3O_4) is a cost-effective and chemically stable catalyst (13) but suffers from limited active site exposure, thereby restricting the formation of heterogeneous Co(IV)=O [≡Co(IV)=O]. Defect engineering, especially anion defects, can create active sites by modulating the coordination environment and electron density of metal sites (14), thus generating reactive species more efficiently and selectively. For example, nitrogen

Significance

The transition metal oxide–activated chlorite process can achieve selective oxidation of organic pollutants by synchronously generating heterogeneous high-valent metal-oxo species and chlorine dioxide. However, heterogeneous high-valent metal-oxo species differ from homogeneous ones in chemical speciation and evolution mechanisms, which are commonly conflated together. Here, photoexcited oxygen vacancies (OVs) were constructed in Co_3O_4 catalysts for promoted chlorite activation. OVs act as "traps" by modulating electronic structures, thereby anchoring O atoms of chlorite and inducing O–Cl cleavage. The electrons near the OV-adjacent Co atom were reassigned after O atom transfer, subsequently generating heterogeneous high-valent cobalt-oxo (≡Co(IV)=O). The revealed oxygen-atom trapping effect will help us revisit the evolution mechanism of surface reactive species in heterogeneous oxidation techniques.

Author contributions: R.S., W.L., and Q.L. designed research; R.S., Y.C., and N.L. performed research; R.S., Y.G., L.C., and B.G. analyzed data; W.L. and B.G. language polishing and visualization; and R.S., Y.C., and N.L. wrote the paper.

The authors declare no competing interest.

This article is a PNAS Direct Submission.

[1]To whom correspondence may be addressed. Email: wen.liu@pku.edu.cn or qianli@sdu.edu.cn.

This article contains supporting information online at https://www.pnas.org/lookup/suppl/doi:10.1073/pnas.2319427121/-/DCSupplemental.

Published March 5, 2024.

vacancies increased the electron density of the Co 3d orbital and decreased the energy barrier for O–O cleavage in peroxymonosulfate (PMS), thus converting the major active species from singlet oxygen ($^1O_2$) to Co(IV)=O (1). In addition, as an intrinsic anion defect, oxygen vacancies (OVs) are rich in localized electrons, thus realizing the exposure of the surface-active sites (15, 16). OVs significantly drove the conversion of unsaturated Co(III)–O_5 sites to highly active Co(IV)–O_6 centers by trapping O atoms from water (17). Therefore, engineering abundant OVs to expose more trapping sites is expected to facilitate the formation of ≡Co(IV)=O for highly efficient chlorite activation. However, there is still insufficient research to elaborate on the evolution mechanism of ≡Co(IV)=O at OV sites.

OVs can be introduced to the catalyst surface by chemical reduction, plasma etching, heteroatom doping, etc. However, OVs are easy to fill by external oxygen atoms (18), leading to the coverage of active sites. Conventional methods for recovering OVs, such as chemical treatments or high-temperature/pressure techniques, are energy-intensive, so how to generate sustainable OVs is essential to the efficient formation of ≡Co(IV)=O. The recent discovery of photoexcited OVs as genuine active sites provides a mild and cost-effective approach to constructing OVs on catalyst surfaces (19, 20). Surface oxygen atoms are highly responsive to the formation of light-induced OVs, which can be restored by re-exposure to light (18). In addition, ultraviolet (UV) irradiation can induce the self-recovery of photoexcited OVs, which can serve as regenerated active sites for subsequent oxygen activation (20). Hence, the photoexcited OVs present an ideal candidate for studying the underlying mechanism of chlorite activation by OVs and also provide an effective engineering strategy to construct sustainable OV sites.

Herein, we constructed OVs into Co_3O_4 via a UV-induced method and fabricated an OV-rich Co_3O_4 (OV-Co_3O_4) catalyst to sustainably produce ≡Co(IV)=O to promote the activation efficiency of chlorite. OV-Co_3O_4 exhibits enhanced activity for the degradation of sulfonamide (SA) antibiotics with a rate constant that is 3.5 times higher than that of pristine Co_3O_4 (p-Co_3O_4). Probe experiments, electron spin resonance (ESR), and UV–Vis absorption spectroscopy confirmed that ≡Co(IV)=O and ClO_2 dominate the oxidative degradation of organics. We identify that OVs can modulate the electronic structure of Co_3O_4 and decrease the O-coordination of the OV-adjacent Co atom, thereby creating an oxygen-atom trapping site for promoted chlorite activation. Density functional theory (DFT) calculations revealed that the formation of ≡Co(IV)=O at OVs is thermodynamically favorable. The stability and sustainability of OV-Co_3O_4 catalysts as well as the oxidative preference of reactive species were evaluated. This work advances the mechanistic understanding of heterogeneous reactive species in AOPs and also presents a feasible strategy for modulating the formation of ≡Co(IV)=O via defect engineering.

Results and Discussion

Characterization of Photoexcited OVs. The preparation process of OV-abundant Co_3O_4 was achieved through a UV-induced method (Fig. 1*A*). The p-Co_3O_4 was obtained by dehydration of the mixture of $Co_2(NO_3)(OH)_3$ and $Co(OH)_2$ (*SI Appendix*, Fig. S1). X-ray diffraction (XRD) patterns (Fig. 1*B*) indicate that the diffraction peaks correspond to the (111), (220), (311), (222), (400), (422), (511), and (440) planes of the cubic Co_3O_4 (JCPDS 42-1467) (21). Field emission-scanning electron microscope (FE-SEM) (*SI Appendix*, Fig. S2) and transmission electron microscope (TEM) (Fig. 1*C*) showed that the OV-Co_3O_4 displayed a cubic crystal with an average size of about 200 nm. High-angle annular dark-field scanning transmission electron microscopy (HAADF-STEM) was further carried out to characterize fine structures. As displayed in Fig. 1*D* and *SI Appendix*, Fig. S3, the interplanar spacings of 2.64 Å and 2.87 Å correspond to the (311) and (220) crystalline planes of cubic Co_3O_4 (JCPDS 42-1467) (22). The HAADF-STEM image of intact Co_3O_4 crystal (*SI Appendix*, Fig. S4) shows regular periodic alignment of lattice Co atoms. After exposure to UV irradiation, the alignment periodicity of lattice Co atoms is disrupted and lattice distortion occurs as marked in Fig. 1*E*. A slight displacement of Co atom was also observed, causing the shortened Co-Co distance (from 5.05 Å to 4.98 Å) compared to the intact Co_3O_4 crystal (*SI Appendix*, Fig. S4). This lattice distortion was ascribed to the existence of vacancies and the formation of unsaturated coordinated metal atoms (23).

The room-temperature ESR of p-Co_3O_4 and OV-Co_3O_4 exhibited a symmetric signal of a Lorentzian shape (*g*-factor = 2.003) (Fig. 1*F*), which originates from the single electrons left at OVs (19). The contents of single electrons were calculated by the double integral of the ESR lines (*SI Appendix*, Table S2). As compared with p-Co_3O_4 (0.03045), the electron contents in OV-Co_3O_4 (0.6196) doubled after 2 h UV irradiation, arising from the promoted generation of photoexcited OVs. However, following another 2-h exposure to UV radiation, no significant rise in electron content was observed due to that the surface OV sites were almost saturated. XPS was further conducted to investigate the valance states of Co and O atoms. In Co 2p XPS spectra (Fig. 1*G*), the two main peaks located at approximately 780.5 and 790.0 eV were attributed to Co $2p_{3/2}$ and Co $2p_{1/2}$, respectively (24). After deconvolution and integration, the increased Co^{2+}/Co^{3+} ratio (from 0.49:1 to 0.89:1) indicated that OVs decreased the valence of cobalt (21, 25). The O 1s XPS spectra (Fig. 1*H*) were deconvoluted into three peaks at 529.8, 531.8, and 532.7 eV, corresponding to the lattice oxygen (O_{latt}), surface adsorbed oxygen (O_{ads}) and oxygen in adsorbed water (O_w), respectively (25, 26). The peak of O_{ads} at 531.8 eV originated from O_2^{2-} or O^- species, which derived from the dissociated molecular oxygen adsorbed at OVs. As compared with that in p-Co_3O_4 (13.88%), the percentage of O_{ads} in OV-Co_3O_4 increased to 28.18%, demonstrating an increase in OV contents.

X-ray absorption fine structure (XAFS) measurements were further conducted to discern the atomic arrangements. As shown Fig. 1*I*, the normalized K-edge X-ray absorption near edge structure (XANES) spectrum of OV-Co_3O_4 at the Co K-edge negatively shifted by 0.4 eV compared with p-Co_3O_4, demonstrating higher electron density around Co in OV-Co_3O_4 than p-Co_3O_4 (16, 27). This is consistent with the deceased valence of Co (from +3 to +2) in XPS spectra. The k^3-weighted Fourier transform (FT) spectra of the Co K-edge extended EXAFS (FT-EXAFS) (Fig. 1*J*) provided information on the coordination environments for Co atoms. The FT curves exhibited three prominent peaks at 1.48 Å, 2.44 Å, and 2.99 Å, which were attributed to the Co-O coordination, Co-Co (octahedral: Oh) and Co-Co (tetrahedral: Td) coordination, respectively (28). The optimized parameters are summarized in *SI Appendix*, Table S3, which were obtained by nonlinear fitting of the Co K-edge EXAFS spectra with least-squares refinement (Fig. 1*K*). The coordination number (CN) in the Co-O coordination shell of OV-Co_3O_4 was reduced to 2.6 compared with that in p-Co_3O_4 (3.0). Interestingly, the Co-O bond length in OV-Co_3O_4 (1.91 Å) was not altered while the CN of Co decreased after UV irradiation. Thus, the coordination environment of Co remained unchanged and the decreased CN was attributed to the escape of surficial oxygen atoms. We

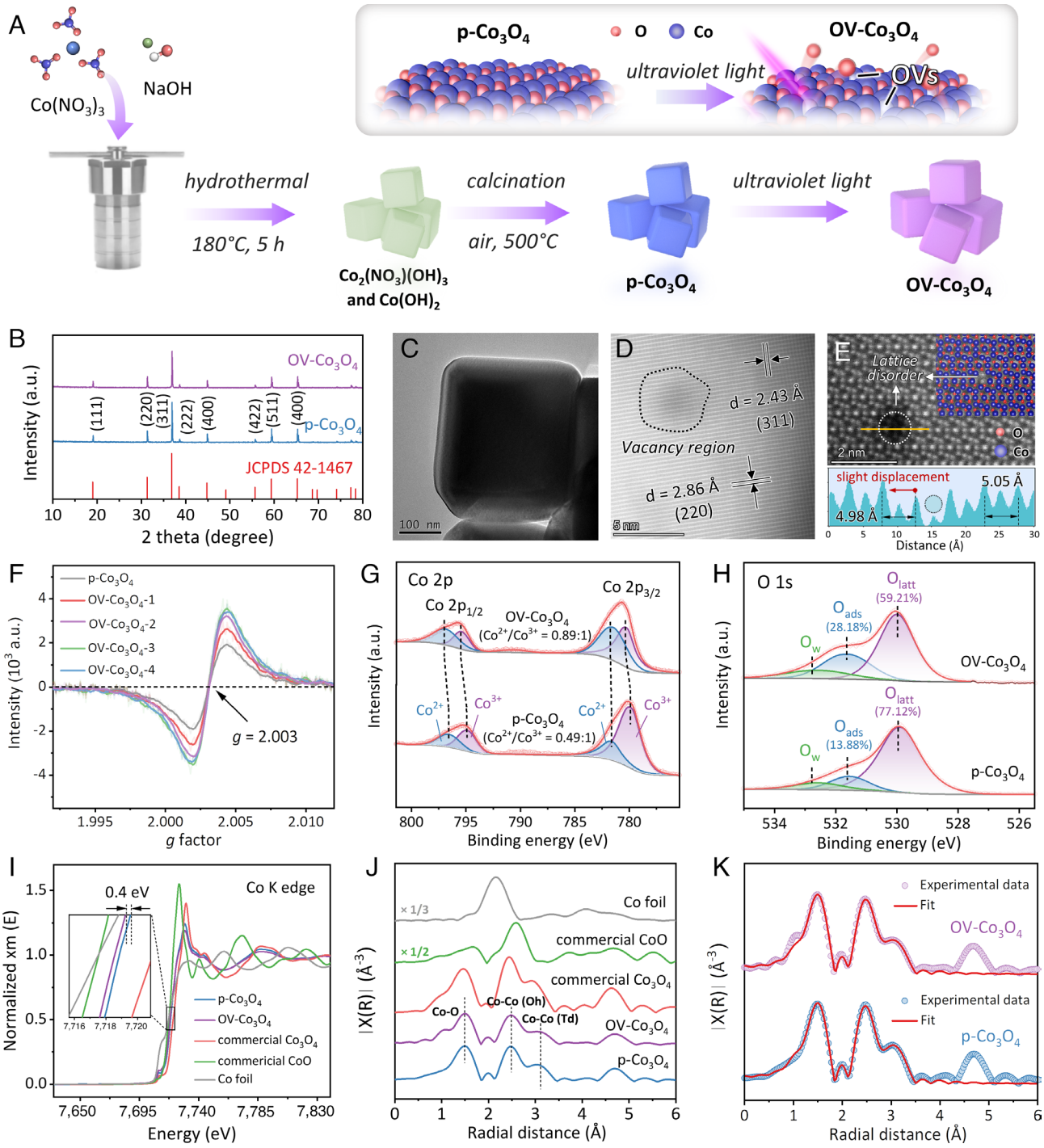

Fig. 1. (*A*) Schematic of the preparation of cubic Co_3O_4 with photoexcited OVs. (*B*) XRD patterns, (*C*) TEM, (*D*) HAADF-STEM, and (*E*) atom-resolution HAADF-STEM images and corresponding structure model of OV-Co_3O_4. (*F*) Time-dependent room-temperature ESR, XPS spectra of (*G*) Co 2p and (*H*) O 1s of p-Co_3O_4 and OV-Co_3O_4. (*I*) Normalized Co K-edge XANES spectra and (*J*) Co *K*-edge FT-EXAFS of different Co materials. (*K*) Co K-edge EXAFS (point) and fit (line) for p-Co_3O_4 and OV-Co_3O_4, shown in k^2 weighted R-space.

also constructed photoexcited OVs in other metal oxides (labeled as OV-M_xO_y) by the UV-induced method. As expected, the degradation efficiencies of SMX in the OV-M_xO_y/chlorite systems were significantly enhanced as compared to that in the M_xO_y/chlorite systems (*SI Appendix*, Fig. S5), suggesting that UV irradiation is a feasible strategy to construct photoexcited OVs for efficient chlorite activation.

Catalytic Activity of OV-Co_3O_4 for Pollutant Oxidation. The catalytic activities of OV-Co_3O_4 catalysts were evaluated by degrading sulfamethoxazole (SMX) and the obvious degradation rate constants (k_{obs}) were obtained by the well-fitted pseudo-first-order kinetic model (*SI Appendix*, Fig. S6*A*). Fig. 2*A* presents that the enhanced activity of OV-Co_3O_4 was closely related to the photoexcited OVs. As compared with the p-Co_3O_4/chlorite process (0.0338 min^{-1}), the values of k_{obs} in the OV-Co_3O_4/chlorite process gradually rose but reached a threshold (~0.1331 min^{-1}) (*SI Appendix*, Fig. S6*B*) due to the almost unchanged OV content after 2 h UV irradiation (*SI Appendix*, Table S2). The k_{obs} values were positively correlated to the dosages of chlorite (R^2 = 0.9990), while the adsorption of SMX onto OV-Co_3O_4 or the oxidative ability of chlorite was negligible (*SI Appendix*,

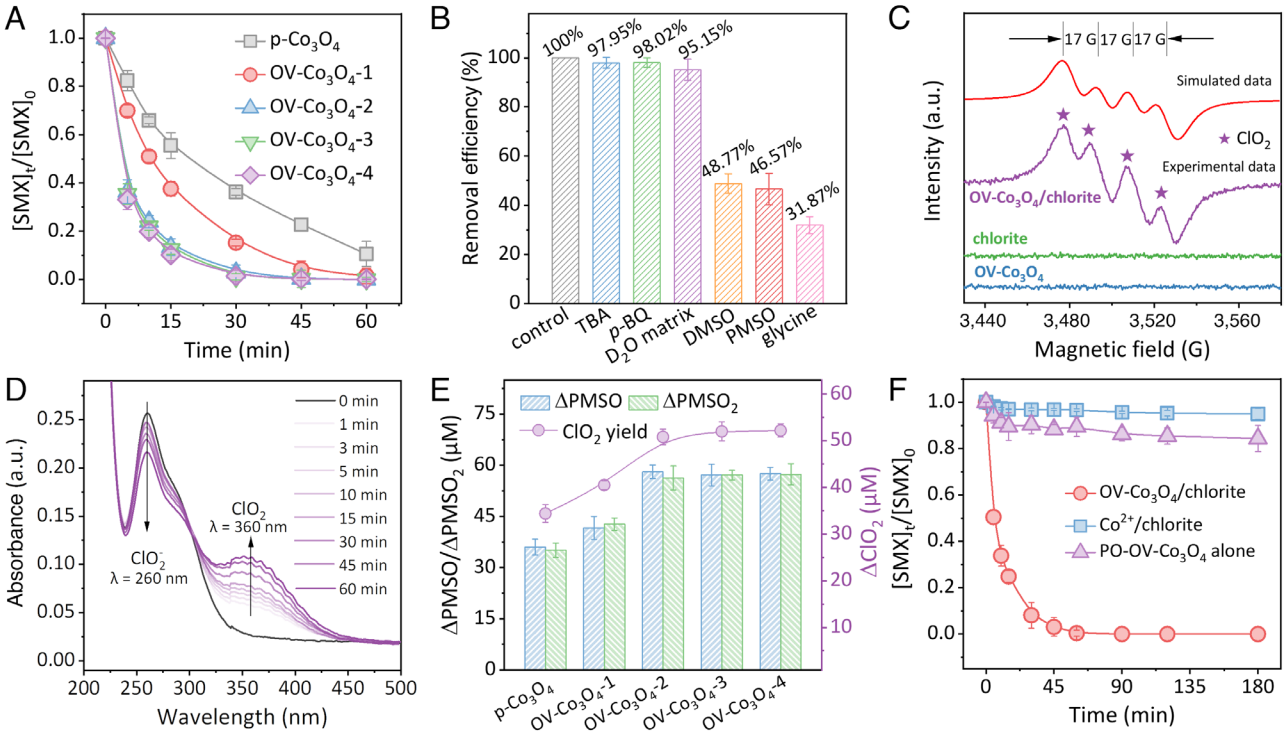

Fig. 2. (*A*) The removal efficiency of SMX in different Co_3O_4/chlorite processes. (*B*) Effects of scavengers on the removal efficiency of SMX. (*C*) ESR spectra of ClO_2, (*D*) time-dependent UV–Vis absorption spectra of ClO_2^-, and (*E*) PMSO consumption, $PMSO_2$ production, and ClO_2 yield in different Co_3O_4/chlorite processes. (*F*) Comparison of removal efficiency of SMX by PO-OV-Co_3O_4 and Co^{2+}/chlorite process.

Fig. S7). Therefore, chlorite was successfully activated to oxidative species for SMX degradation and the activation efficiency greatly depended on the photoexcited OVs.

To identify the reactive oxygen species (ROS), batch quenching tests were carried out using *tert*-butyl alcohol (TBA for $HO^{\cdot}$), *p*-benzoquinone (*p*-BQ for $O_2^{\cdot-}$), and furfuryl alcohol (FFA for $^1O_2$) as quenchers. The addition of TBA nor *p*-BQ exhibited a slight inhibition effect on SMX degradation (Fig. 2*B* and *SI Appendix*, Figs. S8 and S9), indicating the negligible contribution of $HO^{\cdot}$ and $O_2^{\cdot-}$. FFA exerted an obvious inhibition on SMX degradation (*SI Appendix*, Fig. S10), but it was ascribed to the consumption of ClO_2 ($k = 2.45 \times 10^6$ M^{-1} s^{-1}, details shown in *SI Appendix*, Fig. S11) rather than just $^1O_2$. On the other hand, despite the longer lifetime of $^1O_2$ in D_2O (22 to 70 μs) than that in H_2O (2.9 to 4.6 μs) (29), the exchange of solvent from H_2O to D_2O cannot accelerate SMX degradation (Fig. 2*B*), indicating the minor role of $^1O_2$. In addition, the sulfones [i.e., phenyl methyl sulfoxide (PMSO) and dimethyl sulfoxide (DMSO)] exerted an obvious inhibition on SMX degradation (Fig. 2*B* and *SI Appendix*, Figs. S12 and S13), which was ascribed to the unique OAT process between sulfones and Co(IV)=O (30). As a probe of Co(IV)=O, PMSO was converted into its sulfone products $PMSO_2$ and the transformation ratio was approximately 100% (*SI Appendix*, Fig. S14), indicating the presence of Co(IV)=O rather than ROS.

Apart from ROS, it is also necessary to differentiate selective reactive chlorine species (RCS) because the transformation products (TPs) of organic pollutants are closely associated with RCS. For example, ClO_2 generally oxidizes the pollutant through an ET process while free chlorine dominates the chlorination reaction, which would generate undesirable chlorinated by-products. Thus, ESR and quenching tests were conducted to identify the possible RCS during chlorite activation. In Fig. 2*C*, the four-line spectrum with intensities of 1:1:1:1 was assigned to the ClO_2 radical with the hyperfine splitting constant of α_N = 17 G (g = 2.0106 – 2.0108) (31). Besides, the absorbance of ClO_2 at 359 nm (ε_{359} = 1,250 M^{-1} s^{-1}) appeared with decreasing absorbance of ClO_2^- at 254 nm (10), indicating the generation of ClO_2 (Fig. 2*D*). Glycine was further selected as the scavenger for free chlorine ($HClO/ClO^-$) because glycine can react rapidly with free chlorine to form chloro-glycine ($k = 1 \times 10^5$ M^{-1} s^{-1}) (32) but react with ClO_2 slowly ($k = 1 \times 10^{-3}$ M^{-1} s^{-1}) (33). The obvious inhibition of glycine on SMX degradation implied the generation of free chlorine (Fig. 2*B* and *SI Appendix*, Fig. S15). However, the negligible effect on the DPD results indicated the absence of free chlorine (*SI Appendix*, Fig. S16) because glycine would cause a lower result of the DPD quantitative method supposing free chlorine existed. Indeed, the inhibition effect of glycine on SMX degradation derived from the formation of the cobalt–glycine complex (34), suppressing the formation Co(IV)=O (*SI Appendix*, Fig. S17). Another piece of evidence was that no absorbance of free chlorine at 292 nm (ε_{292} = 350 M^{-1} s^{-1}) (35) was detected based on the standard absorption spectrum of free chlorine (*SI Appendix*, Fig. S18), which indicated the negligible generation of free chlorine. Moreover, the sluggish degradation of benzoic acid (BA, the probe for $Cl^{\cdot}$, $k = 5.9 \times 10^9$ M^{-1} s^{-1}) and dimethoxybenzene (DMOB, the probe for $ClO^{\cdot}$, $k = 7.0 \times 10^9$ M^{-1} s^{-1}) showed the negligible generation of $Cl^{\cdot}$ and $ClO^{\cdot}$ (*SI Appendix*, Figs. S19 and S20). Thus, Co(IV)=O and ClO_2 were the dominant reactive species in this OV-Co_3O_4-activated chlorite system, which were quantified by PMSO probe experiments and the DPD quantitative method, respectively. As the OV content saturated (Fig. 1*F*), the amounts of Co(IV)=O and ClO_2 were not significantly increased regardless of prolonged UV irradiation (Fig. 2*E*). The OV-Co_3O_4-2 (hereinafter referred to as OV-Co_3O_4) was selected as the optimal catalyst for further investigation.

During the oxidation of SMX, a trace amount of cobalt leaching (Co^{2+}) in the OV-Co_3O_4/chlorite process was detected (7.943 μg

L^{-1}, ~0.003 wt.%). However, such a low amount of Co^{2+} cannot activate chlorite for efficient removal of SMX (Fig. 2*F*), indicating that heterogeneous reactive species were responsible for pollutant degradation. To clarify the heterogeneous oxidative species, we pre-oxidized OV-Co_3O_4 with chlorite to form Co(IV)=O and then separated the homogeneous oxidative species (i.e., ClO_2 and chlorite) from the pre-oxidized OV-Co_3O_4 (PO-OV-Co_3O_4) (*SI Appendix*, Text S2). In Fig. 2*F*, PO-OV-Co_3O_4 alone can remove 15.64% of SMX in 180 min without the addition of chlorite, implying the presence of heterogeneous reactive species. XPS spectra (*SI Appendix*, Fig. S21) ruled out the possible surface-bound chlorite complex, so the oxidative species was inclined to heterogeneous Co(IV)=O species (≡Co(IV)=O). The generation of ≡Co(IV)=O was also investigated by CV measurements. As shown in *SI Appendix*, Fig. S22, the oxidation peaks of Co^{3+}/Co^{4+} were observed at 1.397 V and 1.371 V (vs. RHE) for p-Co_3O_4 and OV-Co_3O_4, which coincides with the ≡Co(IV)=O in the cobalt-catalyzed processes (36, 37). OV-Co_3O_4 exhibited a lower potential for the Co^{3+}/Co^{4+} oxidation than p-Co_3O_4, showing that OVs facilitated the formation of ≡Co(IV)=O. For catalytic degradation of pollutants, ≡Co(IV)=O exhibited longevity whereby the PO-OV-Co_3O_4 stored for 48 h can still remove about 10% of SMX (*SI Appendix*, Fig. S23). However, when the amount of Co^{2+} (~0.3115 mM) was the same cobalt equivalent as OV-Co_3O_4 (0.25 g L^{-1}), only 5.351% of SMX was removed in the Co^{2+}/chlorite process (*SI Appendix*, Fig. S24) because the unstable homogeneous Co(IV)=O species suffer from strong electronic repulsion between the d-electron of the cobalt center and the electron of oxygen (38). Comparatively, ≡Co(IV)=O species exhibit better stability and higher activity, which allows heterogeneous chlorite activation to accommodate a wider pH range and to resist anion interferences (see *Discussions* in *SI Appendix*, Figs. S25–S28).

Mechanism of the Oxygen-Atom Trapping Effect. DFT calculation is performed to reveal the mechanism of enhanced catalytic activity after the construction of photoexcited OVs. First, the energy of ClO_2^- adsorption at the OV-free site and the OV-adjacent Co site (*SI Appendix*, Fig. S29) are compared to determine the configurations of the adsorbed chlorite. Specifically, the activation of chlorite on the surface of OV-Co_3O_4 includes a two-step ClO_2^- adsorption process. For the first adsorption of ClO_2^-, the O–Cl bond in ClO_2^- is stretched to cleavage (3.00 Å) due to the abundant localized electrons of OV, thus the dissociated O atom (labeled as O*) transfers to coordinate with the surrounding Co atom (Fig. 3*A*). We define the OV-mediated OAT as an "oxygen-atom trapping effect." Comparatively, ClO_2^- is stably adsorbed at the OV-free site with a slightly elongated O–Cl bond (1.96 Å) rather than transferring the O atom to the surface Co atom (*SI Appendix*, Fig. S30). The adsorption of ClO_2^- at the OV-adjacent Co site exhibits more negative adsorption energy (−2.80 eV) than that at the OV-free site (−0.05 eV), suggesting that ClO_2^- prefers to be adsorbed and dissociated at surface OV site, which is more conducive to the formation of ≡Co(IV)=O.

In Fig. 3*B*, the formation of OV gives rise to an increased Bader charge of Co from 7.77 e to 7.89 e (from Co_3O_4 to OV-Co_3O_4), indicating the transition of Co(III) to Co(II) occurs, which is in good accordance with the results of Co 2p XPS spectra (Fig. 1*G*) and Co K-edge XANES spectra (Fig. 1*I*). The first adsorption of ClO_2^- at OV sites leads to decreased Bader charge of Co to 7.69 e (from i to ii in Fig. 3*B*), which are lower than Bader charge of other Co atoms (not OV-adjacent) on the surface, resulting in the formation of ≡Co(IV)=O intermediate. The crystal orbital Hamilton populations (COHP) were calculated to investigate bonding characteristics and ET pathways during the formation of ≡Co(IV)=O. Results of integrals of projected COHP up to the Fermi level revealed that the Co d_{z^2} − Cl bond showed the highest -IpCOHP value (0.891) compared to other Co 3d orbitals (*SI Appendix*, Fig. S31), which indicated the strongest bond strengths of Cl − Co d_{z^2} bond after the first adsorption of ClO_2^-. The -IpCOHP value for Co d_{z^2} − Cl p_z bond (0.695) was higher than those for Co d_{yz} − Cl p_y (0.182) and Co d_{xz} − Cl p_x (0.136) (Fig. 3*C*), verifying that Co d_{z^2} − Cl p_z bond was the dominant channel for d orbital electron transportation. Fig. 3*D* depicts the diagram of bonding and anti-bonding orbitals between the OV-adjacent Co atom and the Cl atom of adsorbed–ClO. To elucidate the oxidation states of the Co site, the projected density of states (PDOS) of the OV-adjacent Co before and after O*-coordination are compared (*SI Appendix*, Fig. S32). The symmetry between spin-up (α-spin) electrons and spin-down (β-spin) electrons decreases, implying the increase of spin electrons (39–41). The amount of spin electrons is further semi-quantitated using the absolute values of the integral difference (|Δ(α-β)|) between α-spin electron and β-spin electron, thereinto, a larger difference represents an increase in spin electrons. After O*-coordination, by comparing the splitting Co-3d orbital PDOS, an obvious increase in spin electrons mostly arises from the electron on the Co-$3d_{xz}$ orbital is extracted by the adsorbed Cl atom, resulting in the higher oxidation state of cobalt.

From the thermodynamic perspective on energy change profiles (Fig. 3*E*), the reaction path of ≡Co(IV)=O is easier to form in the presence of OVs. The highly reactive ≡Co(IV)=O, allows it to accept one electron from the other adsorbed ClO_2^- (O*–ClO_2^{-}*) to generate ClO_2. As shown in Fig. 3*F*, ≡Co(IV)=O can serve as an electron acceptor due to spin single electron and partially unoccupied orbitals of the low energy Co-$3d_{xz}$ and Co − $3d_{z^2}$ orbitals. For the second adsorption of ClO_2^-, the empty Co − $3d_{x^2-y^2}$ orbital can accept lone pair electrons of ClO_2^- to adsorb ClO_2^-, the Bader charge of Co atom increases from 7.69 e to 7.76 e (from ii to iv in Fig. 3*C*), implying the increase of electrons for Co-3d orbitals. Among possible Co d–Cl bonds, the -IpCOHP of Co d_{z^2} − Cl bond was determined to be the highest (0.575) for ≡Co(IV)=O after the second adsorption of ClO_2^- (*SI Appendix*, Fig. S33). The higher value of –IpCOHP indicated that more electrons filled into the bonding orbitals, which was a sign of the formation of a stronger Co-Cl bond. Among Co–Cl bonds, Co d_{z^2} − Cl p_z bond has the highest –IpCOHP value (0.481) (*SI Appendix*, Fig. S34), which serves as the dominant channel for ET. The bonding and anti-bonding orbitals between ≡Co(IV)=O atom and the Cl atom of the second adsorbed ClO_2^- were depicted in *SI Appendix*, Fig. S35. Furthermore, the symmetry between the α-spin electron and the β-spin electron increases (*SI Appendix*, Fig. S36). Compared to those of other Co-3d orbitals, the value of |Δ(α-β)| of Co-$3d_{xz}$ orbital remarkably decreases from 0.287 to 0.077, indicating the decrease in spin electrons for Co-$3d_{xz}$. Thus, the Co-$3d_{xz}$ orbital of ≡Co(IV)=O site undertakes the electron from ClO_2^- to return to a lower oxidation state. The electron loss in ClO_2^- converted the Cl–O sp^3 hybrid into a sp^2 hybrid and left a delocalized electron on the $3p_z$ orbital (Fig. 3 *G* and *H*). Furthermore, a delocalized pi bond (Π^n) is formed between the $3p_z$ electron and the O-2p lone pair electrons, resulting in the shortened O–Cl bond length (1.47 Å) and the relaxed ∠OClO angle (117.6°) (*SI Appendix*, Fig. S37), which well matches the theoretical configuration of ClO_2.

Overall, the heterogeneous chlorite activation undergoes two steps, namely, step (1): OAT and step (2): ET (*SI Appendix*, Fig. S38). First, ClO_2^- is trapped by OV site in OV-Co_3O_4 to

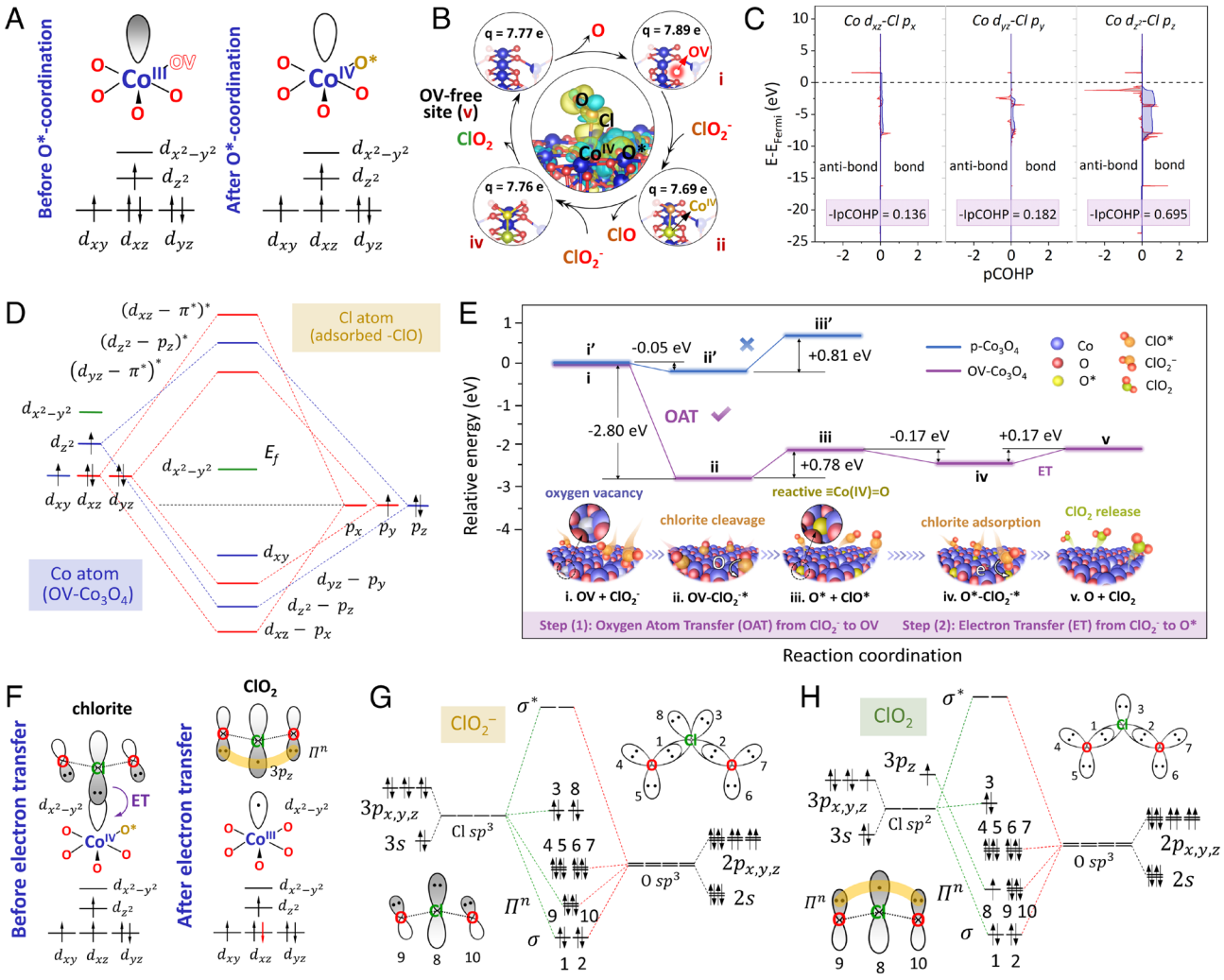

Fig. 3. (*A*) Schematic diagram of Co-3d orbital before and after O*-coordination. (*B*) Bader charge analysis of the formation of ≡Co(IV)=O (cyan stands for holes and yellow for electrons). (*C*) Projected crystal orbital Hamilton populations (pCOHP) and integral -pCOHP (-IpCOHP) of Co d_{xz} – Cl p_x, Co d_{yz} – Cl p_x, and Co d_{z^2} – Cl p_z bonds in OV-Co_3O_4 after first adsorption of ClO_2^-. (*D*) Schematic illustration of bonding and anti-bonding orbitals between OV-adjacent Co atom and the Cl atom of adsorbed –ClO. (*E*) Energy profiles of generation of ≡Co(IV)=O and ClO_2 on OV-free (001) plane and OV-rich (001) plane. Schematic illustrations for the (*F*) ET process from ClO_2^- to ≡Co(IV)=O and the molecular orbitals of (*G*) ClO_2^- and (*H*) ClO_2.

form a metastable ≡Co···O–Cl–O···Co≡ intermediate (Eq. **1**). Second, the abundant localized electrons at OVs induced the O–Cl cleavage, thus generating reactive ≡Co^{IV}–O*–Co≡ species (Eq. **2**). Then, another ClO_2^- is adsorbed onto the O*–Co_3O_4, followed by a fast ET from ClO_2^- to ≡Co^{IV}–O*–Co≡ species, thus inducing the generation of ClO_2 (Eq. **3**). Finally, ≡Co(IV)=O and ClO_2 are jointly responsible for the oxidation of organic pollutants (Eq. **4**). After chlorite activation, OVs would be refilled by picking up O* atom from chlorite, leading to deteriorated performance during recycling (*SI Appendix*, Fig. S39*A*). After the reaction, the filled OVs can be restored by re-exposure to UV light [step (3)], accounting for the revitalized performance of the OV-Co_3O_4/chlorite process (*SI Appendix*, Fig. S39*B*). This phenomenon suggests that the photoexcited OVs can act as sustainable active trapping sites for chlorite activation.

$$\equiv Co\cdots OV\cdots Co\equiv + ClO_2^- \rightarrow \equiv Co\cdots O-Cl-O\cdots Co\equiv, \quad [1]$$

$$\equiv Co\cdots O-Cl-O\cdots Co\equiv \rightarrow \equiv Co^{IV}\cdots O^*\cdots Co\equiv + ClO^*, \quad [2]$$

$$\equiv Co^{IV}\cdots O^*\cdots Co\equiv + ClO_2^- \rightarrow \equiv Co-O-Co\equiv + ClO_2, \quad [3]$$

$$\equiv Co^{IV}\cdots O^*\cdots Co\equiv + ClO_2 + organics \rightarrow oxidation\ products. \quad [4]$$

Selective Degradation of Organic Pollutants. Due to their nucleophile properties, both ≡Co(IV)=O and ClO_2 are prone to selectively attack the electron-rich moieties of SAs. SAs are a class of emerging organic pollutants with aniline moiety (–Ph–NH_2), SA bridge (–SO_2–NH–), and different heterocyclic substituents (*SI Appendix*, Fig. S40) (42). Six SAs were tested as target contaminants, including SA, sulfathiazole (STZ), sulfamethoxazole (SMX), sulfadiazine (SDZ), sulfamerazine (SMZ), and sulfamethazine (SMT). As depicted in Fig. 4*A*, the electron cloud of all the SAs was mainly distributed on the aniline moieties. In the OV-Co_3O_4/chlorite system, the removal efficiencies of the heterocyclic substituents (model compounds) were much lower than that of aniline (*SI Appendix*, Fig. S41), suggesting that aniline is more active than heterocyclic

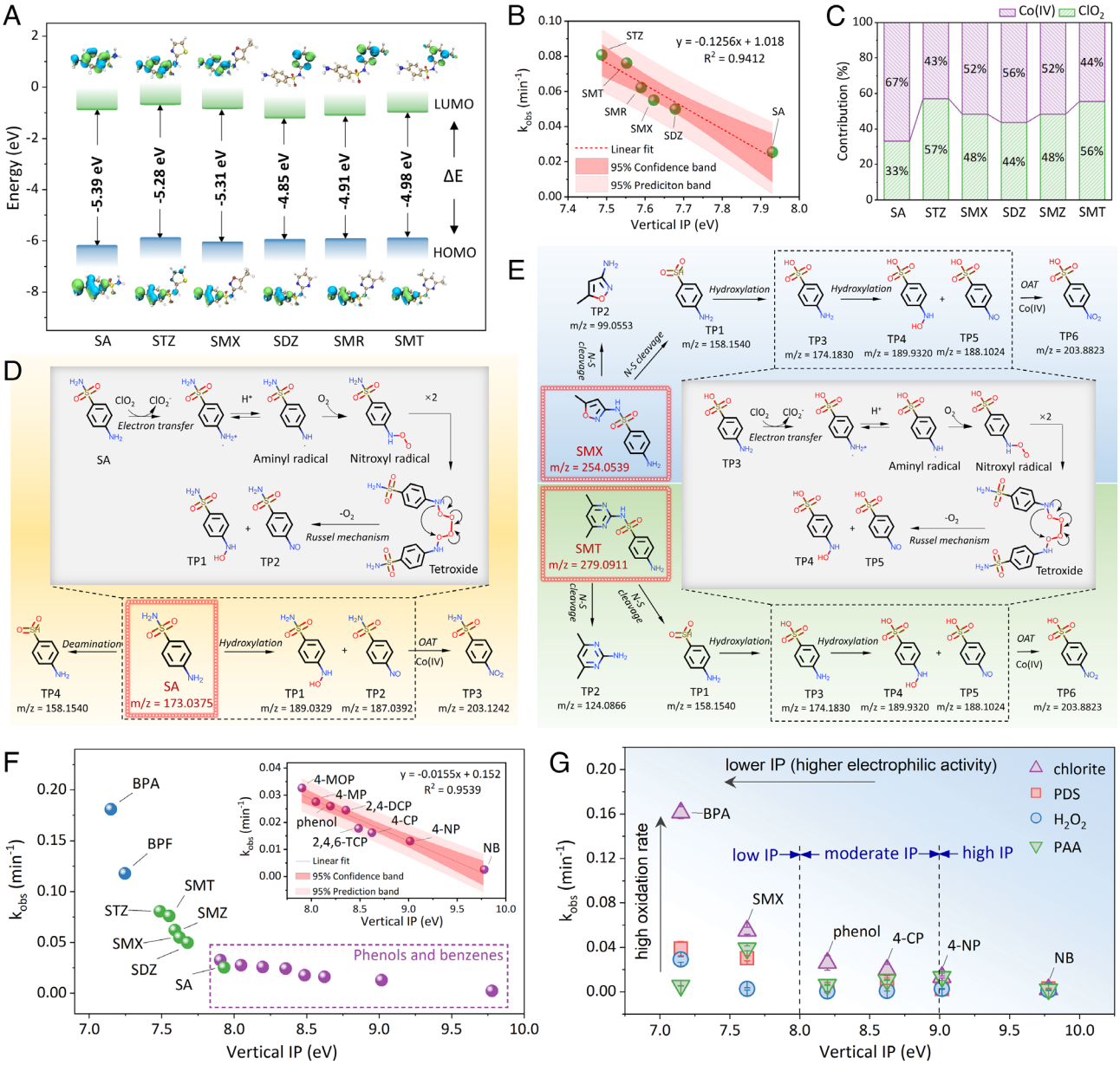

Fig. 4. (*A*) Energy gap between HOMO and LUMO of different SAs. (*B*) Correlation between vertical IP values of SAs and the obvious degradation rate constants (k_{obs}). (*C*) Contributions of ≡Co(IV)=O and ClO_2 to the degradation of SAs at pH 4.0. Degradation pathways of (*D*) SA, (*E*) SMX, and SMT in the OV-Co_3O_4/chlorite process. (*F*) Correlation between vertical IP values of 16 representative pollutants and k_{obs} value. (*G*) Comparison of k_{obs} values of pollutants with different IP values in various oxidation systems. Experimental conditions: [OV-Co_3O_4]$_0$ = 0.25 g L^{-1}, [oxidant]$_0$ = 0.1 mM, [pollutant]$_0$ = 25 μM, pH$_0$ = 4.0 ± 0.3.

substituents. Besides, the heterocyclic substituents increased the reactivity of SAs (*SI Appendix*, Fig. S42), which was reflected by the narrowed energy gap between the highest occupied molecular orbital (HOMO) and the lowest unoccupied molecular orbital (LUMO) $\left(\Delta E = \left|E_{HOMO} - E_{LUMO}\right|\right)$. It is worth noting that the above degradation tests were conducted at pH 4.0 to ensure the SAs zwitterionic (*SI Appendix*, Fig. S26) because the dissociation forms of SAs greatly affected their electrophilic attack activity. Vertical ionization potential (IP), which refers to the required energy to lose one electron, was further selected as the descriptor to evaluate the reactivities of zwitterionic SAs. Generally, the lower vertical IP value represents the higher reactivity of SAs toward electrophilic attack (43). As shown in Fig. 4*B*, the k_{obs} value showed a negative correlation to the IP value, suggesting that the heterocyclic substituents improved the reactivity of SAs toward electrophilic attack. Additionally, the heterocyclic substituents also affected the contribution of reactive species to pollutant degradation (*SI Appendix*, Text S6 and Figs. S43–S45). In Fig. 4*C*, the contribution of ClO_2 to the degradation of SAs with heterocyclic substituents (44 to 57%) was higher than that of SA (33%) because the heterocyclic substituents increased the active sites for ClO_2 oxidation on SA molecules, which will be discussed below.

Condensed Fukui function index (f^-) was further applied to figure out the accurate electrophilic reactive sites on SA molecules. For SA, the aniline-N atom (N11) with the highest f value (f = 0.1485) has the highest nucleophilicity (*SI Appendix*, Table S4), which is vulnerable to electrophilic attacks by ClO_2 and ≡Co(IV)=O. Other SAs with substituents also followed the rule

that the aniline-N atom is the primary reactive site (*SI Appendix*, Tables S5–S9). However, the heterocyclic substituents alter the SA-N atom as the second reactive site, which is reflected by the increased f^- values of SA-N. For example, the f^- value of the SA-N atom of SDZ (N13) (f^- = 0.0528) is higher than that of SA (N14) (f^- = 0.0459), suggesting that the electrons on 5-methylisoxazole moieties are transferred to SA moieties. Therefore, the chlorite activation technique exhibits high selectivity by identifying electrophilic active sites, which are vulnerable to ≡Co(IV)=O and ClO_2.

Furthermore, the transformation products (TPs) of SAs were identified using UPLC-Q-TOF MS (ESI+ mode). For SA, the aniline moiety with the highest f^- value (f^- = 0.1485) was first attacked to form hydroxylamine (TP1, m/z = 189.0329) and nitroso compounds (TP2, m/z = 187.0392) (*SI Appendix*, Fig. S46). In detail, aniline easily accepted one electron from ClO_2 to form aminyl radical (44), which further reacted with oxygen to form a peroxyl radical (Fig. 4*D*). Then, two peroxyl radicals formed a tetroxide and further decayed to hydroxylamine and nitroso compounds via the Russel mechanism (45). In addition, ≡Co(IV)=O also initiated an OAT of the aniline to generate nitroso compounds, which were oxidized to nitro products (TP3, m/z = 203.1242) (30). For heterocyclic substituted SAs (i.e., SMX and SMT), ClO_2 oxidized SMX and SMT through N-S bond cleavage to produce heterocyclic fragments and sulfonic acid products (TP3, m/z = 174.1380) (*SI Appendix*, Figs. S47 and S48). Then, the sulfonic acid products underwent a similar pathway as SA to eventually form nitro-sulfonic acid (TP6, m/z = 203.8823) (dashed box in Fig. 4*E*). Overall, both ≡Co(IV)=O and ClO_2 lead to the oxidation of –Ph–NH_2 and ClO_2 induced the cleavage of –SO_2–NH–. Thus, the contribution of ClO_2 to SAs with heterocyclic substituents was higher compared to that to SA due to the reactive SA bridge. The eco-toxicity of TPs, taking acute and chronic toxicity as indicators, was predicted using the ECOSAR program. In general, most TPs showed lower ecotoxicity than their parent compounds (*SI Appendix*, Tables S10–S12). Thereinto, as compared with that of SA, the toxicity of TPs of SMX and SMT was eliminated more thoroughly because sulfonic acid is more biofriendly than SA.

To elaborate on the selectivity of the chlorite activation process, the underlying relationship between degradation efficiencies and electrophilic properties of 16 representative pollutants was further studied. Pollutants with a lower vertical IP value (higher electrophilic activity) corresponded to a higher degradation rate (Fig. 4*F* and *SI Appendix*, Fig. S42). This indicated that the chlorite activation process was dominated by electrophilic reactions. Moreover, the electrophilic activities of pollutants were closely related to the substituents, which was reflected by the negative linear relationship between k_{obs} and IP value of phenolic and benzene compounds (*Inset* of Fig. 4*F*). Phenolic compounds with electron-donating moieties (such as –OCH_3 and –CH_3) were more inclined to be degraded than those with electron-withdrawing moieties (such as –Cl and –NO_2). Nitrobenzene (NB), merely containing electron-withdrawing –NO_2, showed the lowest degradation efficiency among the selected pollutants (0.0026 min^{-1}). Thus, the chlorite activation process exhibits higher electrophilic selectivity than other AOPs based on peroxides, including hydrogen peroxide (H_2O_2), peroxydisulfate (PDS), and peracetic acid (PAA). To illustrate this superiority, we selected six targeted pollutants, which were categorized as low IP (IP < 8), moderate IP (8 < IP < 9), and high IP (IP > 9) pollutants (*SI Appendix*, Fig. S49). For high IP pollutants (4-nitrophenol (4-NP) and NB), chlorite activation exhibited comparable oxidation capacity to other peroxide activation processes (Fig. 4*G*). However, the degradation efficiencies of moderate and low IP pollutants were higher in chlorite activation systems compared to those in peroxide activation systems. Bisphenol A (BPA) with the lowest IP value (7.15) showed the highest degradation rate in chlorite activation (0.161 min^{-1}), which was about 4.14, 5.53, and 28.8 times higher than those in H_2O_2, PDS, and PAA activation processes, respectively. The superior selectivity arises from the electrophilic reactivity of both ≡Co(IV)=O and ClO_2, which allows chlorite activation as a selective oxidation technique for water decontamination.

Continuous Flow Degradation Tests. In the heterogeneous AOPs, the recovery of catalysts is still a great challenge. For practical application consideration, an OV-Co_3O_4/polyacrylonitrile (PAN) membrane was constructed via electrospinning and the cropped circular membrane (φ = 40 mm, OV-Co_3O_4 loading weight = 17.41 wt.%) was used as the tested membrane (*SI Appendix*, Text S7 and Fig. S50). The SEM image showed that the OV-Co_3O_4/PAN membrane was composed of evenly intertwined fiber composites with a diameter of 400 nm (Fig. 5*A*) and Co elements were uniformly distributed on the fiber (Fig. 5*B*). Compared to the bare PAN membrane, the OV-Co_3O_4/PAN membrane has a larger surface area (232.07 m^2/g) and a denser pore size (92.60 nm) (*SI Appendix*, Table S13). Besides, the hydrophilic OV-Co_3O_4/PAN membrane surface has good wettability with the water contact angle decreased from 59.20° to 13.93° within 30 s (Fig. 5*C*), allowing a good permeation of polluted water.

Furthermore, the continuous flow degradation tests were carried out by sealing the membrane in an Amicon stirred cell model (Fig. 5*D*). The hydraulic retention time (HRT) was determined to be about 6.04 min (*SI Appendix*, Text S8). In ultrapure (UP) water, the SMX removal ratio increased with prolonged membrane-contaminant contact time and reached above 97.5% (Fig. 5*E*). The OV-Co_3O_4/PAN membrane displayed an unremarkable adsorption capacity with a removal ratio of 7.74%, but it exhibited excellent permeability with an average permeance of 565.6 L m^{-2} h^{-1}. Bed volume (BV) tests (*SI Appendix*, Fig. S51) showed that the catalytic reactor retained a high SMX removal efficiency (94.60%) after 240 BV but the permeance dropped to 90% after 120 BV due to the membrane fouling over the limited area. Furthermore, continuous flow degradation tests were performed in actual tap water (TW) and surface water (SW). As shown in *SI Appendix*, Fig. S52, the continuous flow device was able to remove 74.09% of SMX in TW but the removal efficiency fell into a decline (~18.03%) in SW, arising from possible membrane fouling. In SW, the average permeance of the membrane declined to 348.32 L m^{-2} h^{-1}, which reflected the clogged membrane channels and the covered active sites. Thus, the as-described membrane system is suitable for eliminating micropollutants in back-end water treatment cases, such as landscape water and point-of-entry (POE) water purifiers. The Co-leaching was less than 3 μg L^{-1} (Fig. 5*F*), which was far below the reclaimed water limit (50 μg L^{-1}) set by the US Environmental Protection Agency (US EPA). The OV-Co_3O_4/PAN membrane also featured excellent stability with a stable crystalline property (Fig. 5*G*), which guides the design of the catalytic membrane to be integrated into the back-end water purification device.

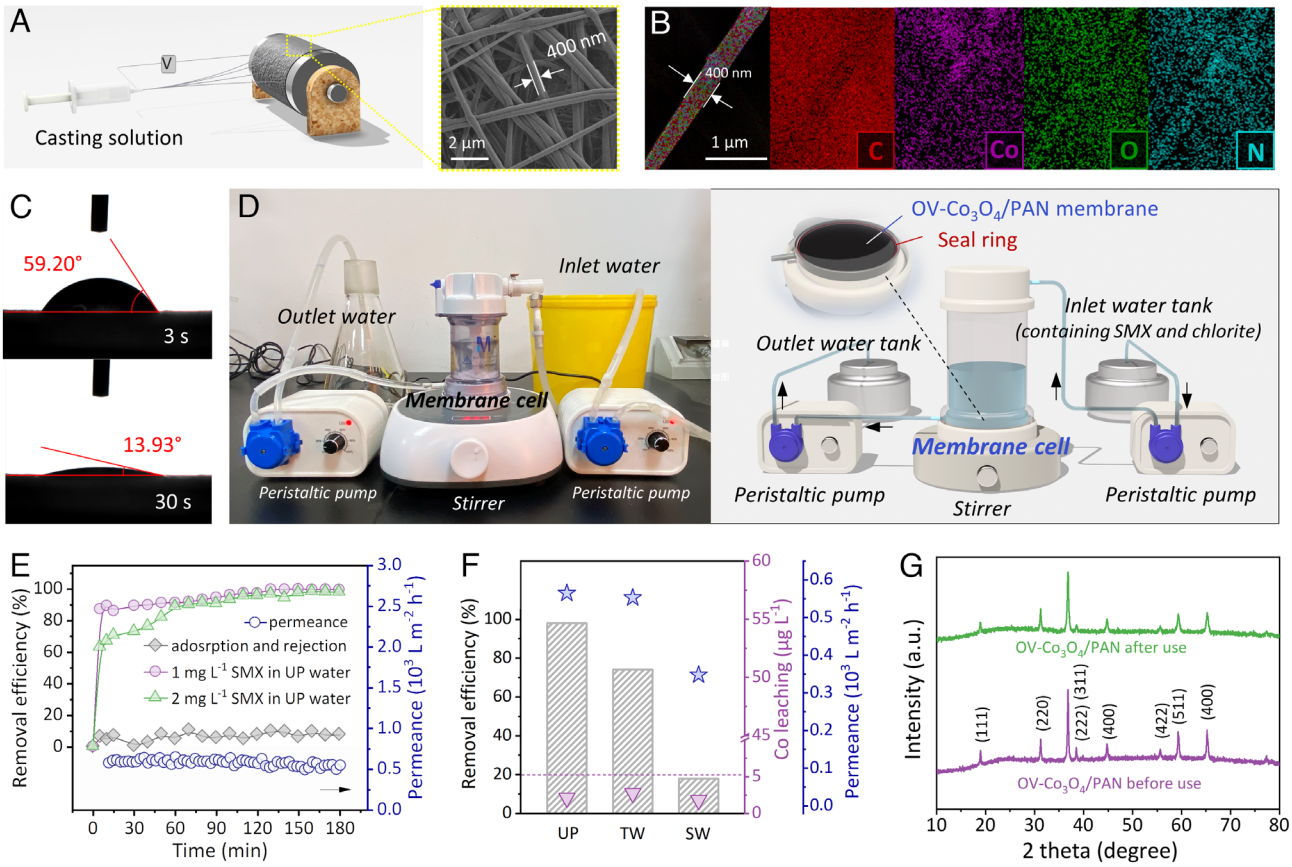

Fig. 5. (*A*) Schematic diagram of electrospinning and SEM image, (*B*) EDS elemental mapping, and (*C*) water contact angle of OV-Co_3O_4/PAN membrane. (*D*) Photograph of the continuous flow degradation experiment with a schematic diagram. SMX removal efficiency and permeance of OV-Co_3O_4/PAN membrane in (*E*) UP water, (*F*) TW, SW, and the cobalt leaking amount. (*G*) XRD patterns of OV-Co_3O_4/PAN membrane before and after use.

Conclusions

In summary, we proposed a strategy to construct photoexcited OVs into Co_3O_4 catalysts (OV-Co_3O_4) via an UV-induced method to promote chlorite activation. X-ray absorption spectroscopy (XAS) and DFT calculations demonstrate that photoexcited OVs modulate the electronic structure of Co_3O_4 and create coordinately unsaturated Co atoms, thereby creating an oxygen-atom trapping site for chlorite adsorption. OV energetically favors the homolytic cleavage of O-Cl bond and the dissociated O* atom is trapped by the OV-adjacent Co atom. The trapped O* atom coordinates with the surrounding Co atom, thereby forming a Co catalytic center in a higher spintronic state ($\equiv Co^{IV}–O^*–Co\equiv$, i.e., $\equiv$Co(IV)=O). Bader charge analysis also revealed the formation of the Co catalytic center in a higher oxidation state after trapping the dissociated O* atom. Due to the low-energy 3d orbitals with unpaired spin electrons, $\equiv$Co(IV)=O extracts one electron from chlorite to form ClO_2. Based on the oxygen-atom trapping effect, OV-Co_3O_4 showed enhanced activity toward chlorite activation and achieved higher efficiency in pollutant degradation than pristine Co_3O_4. Quenching experiments, EPR tests, and spectroscopic techniques show that $\equiv$Co(IV)=O and ClO_2 are jointly responsible for the degradation of pollutants. In addition, due to their electron-deficient properties, $\equiv$Co(IV)=O and ClO_2 are more inclined to attack electron-rich organics, endowing the chlorite technique with high selectivity in water purification. Our work elaborates that OVs facilitate the formation of $\equiv$Co(IV)=O through the oxygen-atom trapping effect, providing a feasible strategy to enhance heterogeneous AOPs by defect engineering.

Materials and Methods

Catalyst Preparation. The pristine Co_3O_4 (p-Co_3O_4) was prepared by a typical hydrothermal method (46) (*SI Appendix*). The p-Co_3O_4 was modified via a UV-induced method to obtain the OV-abundant Co_3O_4, named OV-Co_3O_4. Briefly, 0.5 g of p-Co_3O_4 was evenly tiled on an aluminum foil (φ = 50 mm) and exposed to a UV lamp (200 nm < λ < 420 nm, 100 mW cm^{-2}). A series of OV-Co_3O_4 catalysts were prepared and labeled as OV-Co_3O_4-x [x represents the UV irradiation time (h)]. More details about characterization methods are provided in *SI Appendix*.

Chlorite Activation and Catalyst Activity Evaluation. The chlorite activation activity of OV-Co_3O_4 was studied by degrading SAs in a 100 mL beaker. Specifically, 50 mg of catalyst was first added into 100 mL of SAs solution (25 μM) with vigorous stirring for 30 min to achieve the adsorption-desorption equilibrium. Then, a certain amount of sodium chlorite ($NaClO_2$, 99%) stock solution (10 mM) was added to the solution to reach the initial concentration of chlorite (0.1 to 1.0 mM). Samples (0.5 mL) were withdrawn at specific time intervals and were added 0.5 mL of $Na_2S_2O_3$ (1.0 mM) solution to quench the reactive species. All experiments were performed in duplicate to ensure reproducibility. The concentrations of SAs were measured by high-performance liquid chromatography (HPLC, ThermoFisher, U3000) with detailed conditions listed in *SI Appendix*, Table S1. The degradation intermediates of SAs (ESI+ mode) were identified by ultrahigh performance liquid chromatography-quadrupole time-of-flight premier mass spectrometer (UPLC-Q-TOF MS, ThermoFisher). More details about analytic methods are provided in the *SI Appendix*.

DFT Calculation Details. First-principle calculations were performed by the DFT (47) calculations using the Vienna Ab initio Simulation Package (VASP) with the projector augmented wave (PAW) method. The electronic exchange and correlation effects were treated using the generalized gradient approximation (GGA) with Perdew–Burke–Ernzerhof (PBE). The dispersion energy was corrected by a

Grimme D3 method. The energy cutoff for the plane wave basis expansion was set to 450 eV. The self-consistent calculations apply a convergence energy threshold of 10^{-5} eV, and the force convergency was set to 0.02 eV $Å^{-1}$ for the structure optimization. A vacuum thickness of 15 Å was added to eliminate the interactions between the established slabs. The lattice constants of Co_3O_4 were optimized to be $a = b = c = 8.0821$ Å, in good agreement with the experimental constants. An interstitial OV was introduced to the Co_3O_4 unit cell to build OV-Co_3O_4. The (3 × 3 × 1) Co_3O_4 (110) and (3 × 3 × 1) OV-Co_3O_4 (110) slab with seven atomic layers and a vacuum of 15 Å was built. Atoms in the bottom four atomic layers were fixed to their bulk positions, while the rest were allowed to fully relax. A gamma-centered 3 × 3 × 1 k-point grid was set in the Brillouin zone, while the k-point grid was set to 5 × 5 × 2 for DOS calculation. The Gibbs free energy for the reaction process according to the thermodynamic reaction process, involving two and four elementary reaction steps for Co_3O_4 and OV-Co_3O_4 respectively, was used to evaluate the activity of the Co_3O_4 and OV-Co_3O_4 catalysts. The adsorption energies (E_{ads}) of ClO_2^- for the Co_3O_4 or OV-Co_3O_4 model are calculated using the following equation:

$$E_{ads} = E_{total} - E_{surface} - E_{ClO_2^-}, \quad [5]$$

where E_{total}, $E_{surface}$, and $E_{ClO_2^-}$ are the energy of adsorption configuration, (110) surface of the Co_3O_4 or OV-Co_3O_4 model, and ClO_2^-, respectively. The free energies of the species are calculated as:

$$\Delta G = \Delta E + \Delta ZPE - T\Delta S, \quad [6]$$

where ΔE is the reaction energy of the reactant and product molecules; the zero-point energy (ΔZPE) and entropy ($T\Delta S$) were obtained from the calculation of vibration frequencies for the adsorbed species.

To quantify the reactivity of pollutants, the Fukui function (f^-) based on DFT was performed to predict the reactive sites for electrophilic attacks using Gaussian 09w (48). The geometries and single-point energy of pollutant molecules were calculated at the B3LYP/6-31G* level and were visualized using Multiwfn 3.8 software (49).

Data, Materials, and Software Availability. Full details for chemicals and reagents, material preparation, electrochemical measurements, and calculational details are introduced in *SI Appendix*. All other data are included in the manuscript and/or *SI Appendix*.

ACKNOWLEDGMENTS. This work was financially supported by the National Natural Science Foundation of China (52070121, U22A20423, and 52270053) and the Taishan Scholars Foundation of Shandong Province (Q.L.). This work was also supported by grants from the National Key Research and Development Program of China (2021YFA1202500), the Major Program of Shandong Province Technological Innovation Project (No. 2020CXGC011403), the Beijing Nova Program (No. 20220484215), and the Beijing Natural Science Foundation (No. 8232035). Supports from the Analytical Testing Center of School of Environmental Science and Engineering of Shandong University, the State Key Laboratory of Microbial Technology of Shandong University, the Beamlines MCD-B (Soochow Beamline for Energy Materials) and Fourier transform infrared spectrometer (Bruker IFS 66v) on the infrared beamline (BL01B) at National Synchrotron Radiation Laboratory of China, Shanghai Synchrotron Radiation Facility (Instrument BL11B), the 1W1B station at Beijing Synchrotron Radiation Facility, the High-Performance Computing Platform of Peking University, are also greatly acknowledged.

Author affiliations: [a]Shandong Provincial Key Laboratory of Water Pollution Control and Resource Reuse, Shandong Key Laboratory of Environmental Processes and Health, School of Environmental Science and Engineering, Shandong University, Qingdao, Shandong 266237, People's Republic of China; [b]College of Environmental Sciences and Engineering, State Environmental Protection Key Laboratory of All Material Fluxes in River Ecosystems, Peking University, Beijing 100871, People's Republic of China; and [c]College of Environment and Safety Engineering, Qingdao University of Science and Technology, Qingdao, Shandong 266042, People's Republic of China

1. J. Jiang *et al.*, Nitrogen vacancy-modulated peroxymonosulfate nonradical activation for organic contaminant removal via high-valent cobalt-oxo species. *Environ. Sci. Technol.* **56**, 5611–5619 (2022).
2. Y. Wei *et al.*, Ultrahigh peroxymonosulfate utilization efficiency over CuO nanosheets via heterogeneous Cu(III) formation and preferential electron transfer during degradation of phenols. *Environ. Sci. Technol.* **56**, 8984–8992 (2022).
3. H. Li, C. Shan, B. Pan, Fe(III)-doped g-C_3N_4 mediated peroxymonosulfate activation for selective degradation of phenolic compounds via high-valent iron-oxo species. *Environ. Sci. Technol.* **52**, 2197–2205 (2018).
4. Y. Bao *et al.*, Generating high-valent Iron-oxo ≡Fe^{IV}=O Complexes in neutral microenvironments through peroxymonosulfate activation by Zn−Fe layered double hydroxides. *Angew. Chem. Int. Ed. Engl.* **61**, e2022095 (2022).
5. W. Ren *et al.*, Insights into the electron-transfer regime of peroxydisulfate activation on carbon nanotubes: The role of oxygen functional groups. *Environ. Sci. Technol.* **54**, 1267–1275 (2020).
6. Y. Gao *et al.*, Intrinsic properties of biochar for electron transfer. *Chem. Eng. J.* **475**, 146356 (2023).
7. Q. Y. Wu, Z. W. Yang, Z. W. Wang, W. L. Wang, Oxygen doping of cobalt-single-atom coordination enhances peroxymonosulfate activation and high-valent cobalt-oxo species formation. *Proc. Natl. Acad. Sci. U.S.A.* **120**, e2219923120 (2023).
8. I. Schaffner *et al.*, Molecular mechanism of enzymatic chlorite detoxification: Insights from structural and kinetic studies. *ACS Catal.* **7**, 7962–7976 (2017).
9. R. Su *et al.*, Revealing the generation of high-valent cobalt species and chlorine dioxide in the Co_3O_4-activated chlorite process: Insight into the proton enhancement effect. *Environ. Sci. Technol.* **57**, 1882–1893 (2023).
10. S. D. Hicks *et al.*, Non-heme manganese catalysts for on-demand production of chlorine dioxide in water and under mild conditions. *J. Am. Chem. Soc.* **136**, 3680–3686 (2014).
11. A. Ali, W. Akram, H. Y. Liu, Reactive cobalt-oxo complexes of tetrapyrrolic macrocycles and N-based ligand in oxidative transformation reactions. *Molecules* **24**, 24010078 (2018).
12. H. Li, N. Yuan, J. Qian, B. Pan, Mn_2O_3 as an electron shuttle between peroxymonosulfate and organic pollutants: The dominant role of surface reactive Mn(IV) species. *Environ. Sci. Technol.* **56**, 4498–4506 (2022).
13. K. Zha, W. Sun, Z. Huang, H. Xu, W. Shen, Insights into high-performance monolith catalysts of Co_3O_4 nanowires grown on nickel foam with abundant oxygen vacancies for formaldehyde oxidation. *ACS Catal.* **10**, 12127–12138 (2020).
14. Z. Wei *et al.*, Oxygen vacancy-engineered titanium-based perovskite for boosting H_2O activation and lower-temperature hydrolysis of organic sulfur. *Proc. Natl. Acad. Sci. U.S.A.* **120**, e2217148120 (2023).
15. H. Shang *et al.*, Oxygen vacancies promoted the selective photocatalytic removal of NO with Blue TiO_2 via simultaneous molecular oxygen activation and photogenerated hole annihilation. *Environ. Sci. Technol.* **53**, 6444–6453 (2019).
16. Z. Xiao *et al.*, Operando identification of the dynamic behavior of oxygen vacancy-rich Co_3O_4 for oxygen evolution reaction. *J. Am. Chem. Soc.* **142**, 12087–12095 (2020).
17. E. L. Tae *et al.*, Cobalt oxide electrode doped with iridium oxide as highly efficient water oxidation electrode. *ACS Catal.* **5**, 5525–5529 (2015).
18. S. Wang *et al.*, Light-switchable oxygen vacancies in ultrafine Bi_5O_7Br nanotubes for boosting solar-driven nitrogen fixation in pure water. *Adv. Mater.* **29**, 1701774 (2017).
19. Q. Ren, Y. He, H. Wang, Y. Sun, F. Dong, Photo-switchable oxygen vacancy as the dynamic active site in the photocatalytic NO oxidation reaction. *ACS Catal.* **12**, 14015–14025 (2022).
20. Y. He *et al.*, Operando identification of dynamic photoexcited oxygen vacancies as true catalytic active sites. *ACS Catal.* **13**, 191–203 (2022).
21. Y. Liu *et al.*, Efficient selective oxidation of aromatic alkanes by double cobalt active sites over oxygen vacancy-rich mesoporous Co_3O_4. *Angew. Chem. Int. Ed. Engl.* **62**, e202306261 (2023), 10.1002/anie.202306261.
22. Y. Chen *et al.*, Crystal plane effect of Co_3O_4 on Styrene catalytic oxidation: Insights into the role of Co^{3+} and oxygen mobility at diverse temperatures. *ACS Appl. Mater. Interfaces* **15**, 32404–32415 (2023), 10.1021/acsami.3c04731.
23. S. Chen *et al.*, Oxygen vacancy associated single-electron transfer for photofixation of CO_2 to long-chain chemicals. *Nat. Commun.* **10**, 788 (2019).
24. C. Song *et al.*, Overturned loading of inert CeO_2 to active Co_3O_4 for unusually improved catalytic activity in fenton-like reactions. *Angew. Chem. Int. Ed. Engl.* **61**, e202200406 (2022), 10.1002/anie.202200406.
25. S. Wang *et al.*, Oxygen vacancy-mediated CuCoFe/tartrate-LDH catalyst directly activates oxygen to produce superoxide radicals: Transformation of active species and implication for nitrobenzene degradation. *Environ. Sci. Technol.* **56**, 7924–7934 (2022).
26. J. Bae *et al.*, Facet-dependent Mn doping on shaped Co_3O_4 crystals for catalytic oxidation. *ACS Catal.* **11**, 11066–11074 (2021).
27. W. Zhong *et al.*, Oxygen vacancies induced by charge compensation tailoring Ni-doped Co_3O_4 nanoflakes for efficient hydrogen evolution. *Chem. Eng. J.* **436**, 134813 (2022).
28. Z. Xiao *et al.*, Filling the oxygen vacancies in Co_3O_4 with phosphorus: An ultra-efficient electrocatalyst for overall water splitting. *Energy Environ. Sci.* **10**, 2563–2569 (2017).
29. F. Wilkinson, J. G. Brummer, Rate constant for the decay and reactions of the lowest electronically excited singlet-state of molecular-oxygen in solution. *J. Phys. Chem. Ref. Data* **10**, 809–1000 (1981).
30. Y. Zong *et al.*, Unraveling the overlooked involvement of high-valent cobalt-oxo species generated from the Cobalt(II)-activated peroxymonosulfate process. *Environ. Sci. Technol.* **54**, 16231–16239 (2020).
31. J. Marcon *et al.*, New insights into the decomposition mechanism of chlorine dioxide at alkaline pH. *Holzforschung* **71**, 599–610 (2017).
32. D. I. Pattison, M. J. Davies, Absolute rate constants for the reaction of hypochlorous acid with protein side chains and peptide bonds. *Chem. Res. Toxicol.* **14**, 1453–1464 (2001).
33. J. Hoigne, H. Bader, Kinetics of reactions of chlorine dioxide (OCLO) in water. 1. Rate constants for inorganic and organic-compounds. *Water Res.* **28**, 45–55 (1994).
34. L. Jiang, Y. He, Y. Li, Y. Li, J. Luo, Synergetic effect of H_2O_2 and glycine on cobalt CMP in weakly alkaline slurry. *Microelectron. Eng.* **122**, 82–86 (2014).

35. M. S. Abdighahroudi, T. C. Schmidt, H. V. Lutze, Determination of free chlorine based on ion chromatography-application of glycine as a selective scavenger. *Anal. Bioanal. Chem.* **412**, 7713–7722 (2020).
36. N. Yao *et al.*, Intermolecular energy gap-induced formation of high-valent cobalt species in CoOOH surface layer on cobalt sulfides for efficient water oxidation. *Angew. Chem. Int. Ed. Engl.* **61**, e202117178 (2022).
37. J. Song *et al.*, Asymmetrically coordinated CoB_1N_3 moieties for selective generation of high-valence Co-oxo species via coupled electron-proton transfer in fenton-like reactions. *Adv. Mater.* **35**, e2209552 (2023), 10.1002/adma.202209552.
38. A. Ali, W. Akram, H. Y. Liu, Reactive cobalt(-)oxo complexes of tetrapyrrolic macrocycles and N-based ligand in oxidative transformation reactions. *Molecules* **24**, 78 (2018).
39. W. Zhong *et al.*, Electronic spin moment as a catalytic descriptor for Fe single-atom catalysts supported on C_2N. *J. Am. Chem. Soc.* **143**, 4405–4413 (2021).
40. Q. Dang *et al.*, Regulating electronic spin moments of single-atom catalyst sites via single-atom promoter tuning on S-vacancy MoS_2 for efficient nitrogen fixation. *J. Phys. Chem. Lett.* **12**, 8355–8362 (2021).
41. Q.-K. Li, X.-F. Li, G. Zhang, J. Jiang, Cooperative spin transition of monodispersed FeN_3 sites within graphene induced by CO adsorption. *J. Am. Chem. Soc.* **140**, 15149–15152 (2018).
42. J. Hu *et al.*, Comparison of chemical and biological degradation of sulfonamides: Solving the mystery of sulfonamide transformation. *J. Hazard. Mater.* **424**, 127661 (2022).
43. L. Zhang *et al.*, Highly efficient activation of peracetic acid by nano-CuO for carbamazepine degradation in wastewater: The significant role of H_2O_2 and evidence of acetylperoxy radical contribution. *Water Res.* **216**, 118322 (2022).
44. W. Gan, Y. Ge, Y. Zhong, X. Yang, The reactions of chlorine dioxide with inorganic and organic compounds in water treatment: Kinetics and mechanisms. *Environ. Sci. Water Res. Technol.* **6**, 2287–2312 (2020).
45. S. Willach *et al.*, Degradation of sulfamethoxazole using ozone and chlorine dioxide-compound-specific stable isotope analysis, transformation product analysis and mechanistic aspects. *Water Res.* **122**, 280–289 (2017).
46. X. Xiao *et al.*, Facile shape control of Co_3O_4 and the effect of the crystal plane on electrochemical performance. *Adv. Mater.* **24**, 5762–5766 (2012).
47. G. Seifert, D. Porezag, T. Frauenheim, Calculations of molecules, clusters, and solids with a simplified LCAO-DFT-LDA scheme. *Int. J. Quant. Chem.* **58**, 185–192 (1996).
48. M. J. Frisch *et al.*, Gaussian (Gaussian 16, Revision B.01, Gaussian, Inc., Wallingford, CT, 2016).
49. T. Lu, F. W. Chen, Multiwfn: A multifunctional wavefunction analyzer. *J. Comput. Chem.* **33**, 580–592 (2012).